PASJ: Publ. Astron. Soc. Japan **54**, 819–832, 2002 December 25

FOCAS: The Faint Object Camera and Spectrograph for the Subaru Telescope

Nobunari KASHIKAWA,[1,2] Kentaro AOKI,[3] Ryo ASAI,[4] Noboru EBIZUKA,[5] Motoko INATA,[1]
Masanori IYE,[1,2] Koji S. KAWABATA,[1] George KOSUGI,[3] Youichi OHYAMA,[3] Kiichi OKITA,[1]
Tomohiko OZAWA,[6] Yoshihiko SAITO,[4] Toshiyuki SASAKI,[3] Kazuhiro SEKIGUCHI,[3]
Yasuhiro SHIMIZU,[7] Hiroko TAGUCHI,[8] Tadafumi TAKATA,[3]
Yasushi YADOUMARU,[6] and Michitoshi YOSHIDA[1,7]
[1]*Optical and Infrared Astronomy Division, National Astronomical Observatory, Mitaka, Tokyo 181-8588*
kashik@zone.mtk.nao.ac.jp
[2]*Department of Astronomy, School of Science, Graduate University for Advanced Studies, Mitaka, Tokyo 181-8588*
[3]*Subaru Telescope, National Astronomical Observatory, 650 North A'ohoku Place, Hilo, HI 96720, USA*
[4]*Department of Astronomy, School of Science, The University of Tokyo, Bunkyo-ku, Tokyo 113-0033*
[5]*Communications Research Laboratory, Koganei, Tokyo 184-8795*
[6]*Misato Observatory, Misato, Wakayama 640-1366*
[7]*Okayama Astrophysical Observatory, National Astronomical Observatory, Kamogata, Okayama 719-0232*
[8]*Department of Astronomy and Earth Sciences, Tokyo Gakugei University, Koganei, Tokyo 184-8501*

(Received 2002 June 26; accepted 2002 September 11)

Abstract

The Faint Object Camera and Spectrograph (FOCAS) is a Cassegrain optical instrument for the Subaru Telescope. Its capabilities include $6'\phi$ FOV direct imaging, low-resolution spectroscopy (R = 250–2000 with $0.''4$ slitwidth), multi-slit spectroscopy and polarimetry. We describe the overall design of FOCAS, its observing functions, and the performance verification procedures that have been carried out.

Key words: instrumentation: spectrographs

1. Introduction

The Faint Object Camera and Spectrograph (FOCAS) is one of the seven common-use facility instruments of the 8.2-m Subaru Telescope (Kaifu et al. 2000) on Mauna Kea. The basic concept of FOCAS, as a versatile Cassegrain optical instrument for imaging and low- to medium-resolution multi-object spectroscopy, was proposed in the late 80's. Together with the wide-field prime-focus camera (Suprime-Cam) and the high-dispersion spectrograph (HDS), it was intended to form part of a suite of optical instruments for the Subaru Telescope. Since FOCAS allows broad- and narrow-band imaging, spectroscopy, imaging polarimetry, and spectropolarimetry of a wide range of objects, the science objectives include studies of faint objects in the solar system, faint stars, nebulae, and star clusters in the Galaxy, individual objects in nearby galaxies, the internal structure of galaxies, spectroscopic studies of active galactic nuclei, the evolution of clusters of galaxies, high-redshift quasars, and so on.

Various design and development efforts were made between 1991 and 1995 to finalize the detailed design of FOCAS (Iye 1994; Sasaki et al. 1994). Among the items developed and optimized were the optical design, the mechanical design, the control system, the CCD camera electronics, the structure of the dewar, the multi-slit exchange mechanism, the multi-slit fabrication system, the multi-layer anti-reflective coating, the filters, the grisms, the wave plates for polarimetry, and so on. A great deal of practical experience, which was useful in defining the control system of FOCAS, was obtained during the fabrication and installation of the Okayama Optical Polarimetry and Spectroscopy system (OOPS) on the Okayama 91-cm telescope in the early 90's. Construction of FOCAS started in 1996, and the system was shipped to Hawaii in 1999. Action and control tests, adjustments, and optimizations were carried out using the two common-use telescope simulators installed at the Mitaka campus in Tokyo and at the Hilo base facility of NAOJ. First light on FOCAS (Kashikawa et al. 2000; Yoshida et al. 2000) was obtained in 2000 February (figure 1). Since FOCAS is a sophisticated instrument with various modes of observation, it took another year and a half to commission and test all of the instrument's features, including the multi-object spectrograph capability, but not including the polarimetric capability. FOCAS has been available for common-use observations since 2001 April. The polarimetry mode, which has been tested since 2002 February, is intended to be available after 2003 April. In this paper, we describe the overall design and observing functions of FOCAS and the performance verification procedures that have been carried out. Further information on the instrument can be found at ⟨http://www.naoj.org/Observing/Instruments/FOCAS/⟩.

2. The Optics of FOCAS

2.1. The Main Optics Train

FOCAS is mounted at the F12.2 Cassegrain focus of the 8.2-m Subaru Telescope, where the image scale is $2.''06\,\mathrm{mm}^{-1}$ given the telescope focal length of 100 m. It has a field curvature with a radius of 2409 mm, due to the Ritchey–Chrétien design of the Subaru Telescope. FOCAS is designed to cover the entire unvignetted region of the Cassegrain FOV, $6'$ in diameter.

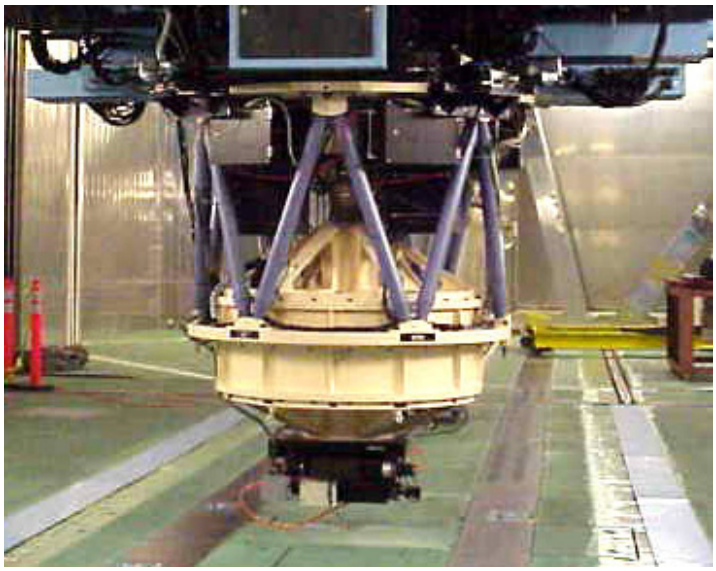

Fig. 1. FOCAS mounted at the Cassegrain focus of the 8.2-m Subaru Telescope.

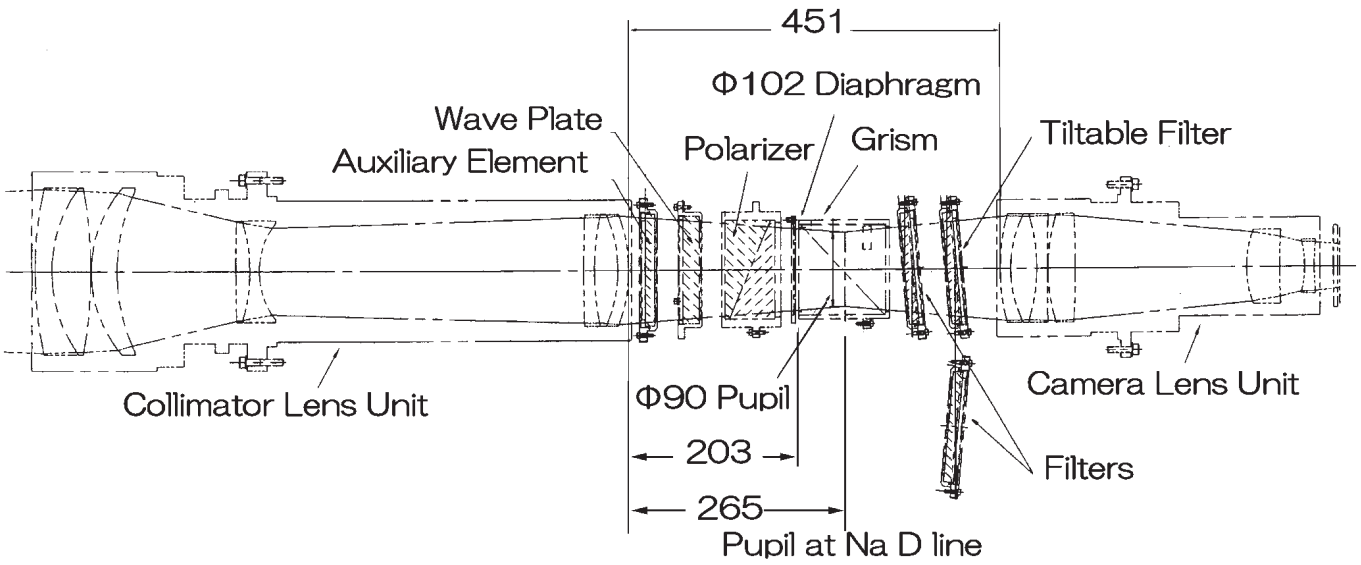

Fig. 2. Optical train of the main optics of FOCAS. The collimator part consists of 8 elements in 4 groups, while the camera part consists of 6 elements in 4 groups. The turret section contains various optical elements.

The focal reducing optics maps the telescope focal plane onto a pair of $4\,\mathrm{K} \times 2\,\mathrm{K}$ CCDs with 15 μm pixel size at a pixel scale of $0\farcs1$/pix. The transmitting optics consists of a collimator lens unit and a camera lens unit, manufactured by NIKON Co. (figure 2). The collimator lens unit consists of 8 lenses with 8 surfaces and has a focal length of 1097.7 mm, while the camera lens unit consists of 6 lenses with 8 surfaces and has a focal length of 329.4 mm. The pupil of the optical system is 90 mm in diameter and the focal reduction factor is 3/10. A rigorous effort to optimize the optical design of the relay lens system allowed the inclusion of a collimated beam section, 451 mm in length, between the collimator lens unit and the camera lens unit, where grisms, filters, and polarizers can be inserted.

2.2. *Transmission and Image Quality*

The optical design was optimized for the wavelength region between 365–900 nm; the multi-layer anti-reflection coatings on the lens surfaces enable a high transmission, exceeding 80%, for wavelengths of between 420–900 mm, as shown in figure 3. The throughput in the ultraviolet is limited by the transmittance of the glass materials; the measured transmittance is 65% at 365 nm and 30% at 350 nm.

The r.m.s. diameter of the PSF, averaged over the optimized wavelength range, has been found to be as small as $0\farcs11$ at the field center and smaller than $0\farcs14$ over the field of view (figure 4).

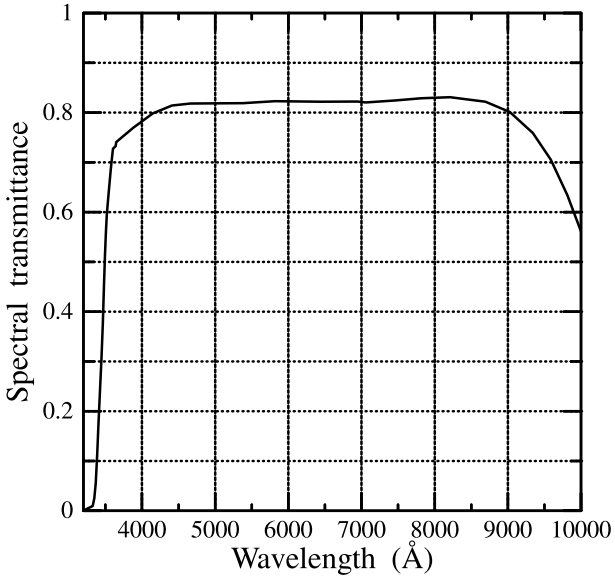

Fig. 3. Designed efficiency curves of the FOCAS main optical train.

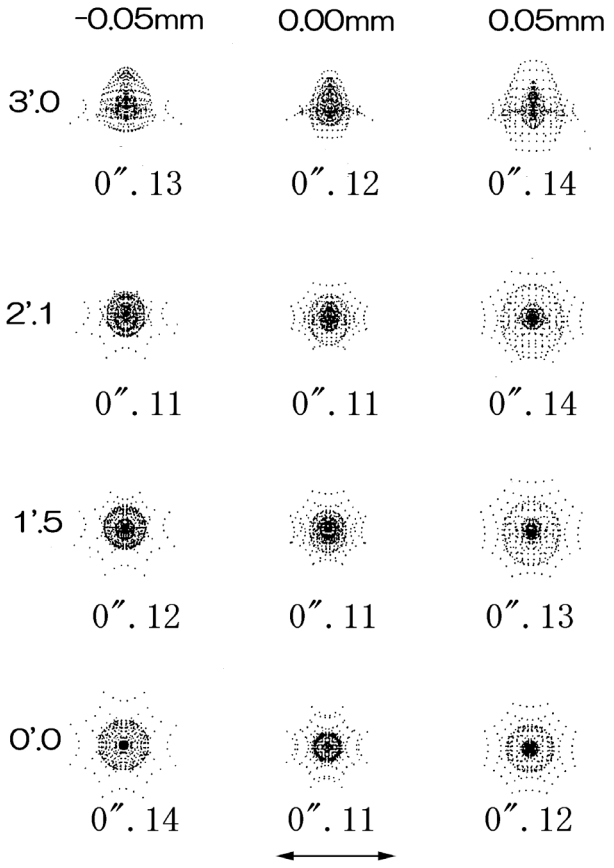

Fig. 4. Spot diagrams of the optics, as designed. The spots are a weighted average over the optimized wavelength region, 365–900 nm. The spot diagrams at the field center (bottom row) to the field edge at 3′ away (top row) are shown for the on-focus position (central column) and defocused positions (right and left columns). The arrow at the bottom denotes 0.05 mm on the CCD plane.

2.3. Grisms, Filters, and Polarizers

Table 1 summarizes the full set of grisms that are currently available. We characterize their properties by $R = \lambda/\Delta\lambda$, assuming a slit width of 0.″4. By the end of 2002, FOCAS will be equipped with nine grisms optimized for different resolving powers, from $R = 250$ up to $R = 5000$ over appropriate wavelength ranges. However, for the moment, only four grisms are available: a very low-dispersion ($R \sim 250$, 75 grooves mm^{-1}) grism, a low-dispersion ($R \sim 500$, 150 grooves mm^{-1}) grism, two medium-dispersion ($R \sim 1000$, 300 grooves mm^{-1}) grisms for the blue and the red spectral regions, and an echelle-type grism covering most of the optical wavelengths at the second, third, fourth, and fifth orders. These are made by the conventional process of replication onto a glass prism of refractive index ~ 1.5. The entrance aperture size of the grisms is 105 mm × 105 mm. The measured efficiencies are 80%, 78%, 82%, and 65% at the blazed wavelength for the very low, low, medium (blue), and medium (red) dispersion grisms respectively. The efficiency of the echelle grism is 65% to 75% at direct visible wavelengths at each order, as shown in figure 5. Two more conventional 600 grooves mm^{-1} grisms for the blue (B to V) and the red (R) regions for high-dispersion spectroscopy ($R \gtrsim 1000$) are currently under fabrication. In addition to these grisms, we are developing two new types of high-dispersion volume phase holographic (VPH) grisms for the U to B bands and for the I band. These VPH grisms consist of a VPH grating of photosensitive resin sandwiched between two prisms of conventional optical glass, and provide higher efficiencies than conventional grisms. Research and development efforts were made to utilize prisms made of high refractive index materials in order to obtain very high dispersion grisms, with resolving power exceeding 10000, and are continuing (Ebizuka et al. 2000).

A standard set of Johnson–Cousins $UBVRI$ broad-band filters, as well as the SDSS $u'g'r'i'z'$ filters, are available for imaging. The filters are 130 mm ϕ × 10 mm in size. LC50, SO58, SY47, and L600 filters should be used for spectroscopic modes to avoid order mixing. For emission-line imaging observations, some narrow-band filters for the most commonly observed emission lines are available.

For polarimetric observations, a half-wave plate, a quarter-wave plate and a Wollaston prism manufactured by B. Halle Nachfl. are available. Both of the wave plates are Pancharatnam-type super-achromatic retarders, and the deviation of the retardations is less than 3° in the wavelength range between 3500 Å and 12000 Å (figure 6). The crystal quartz Wollaston prism, consisting of three elements, splits the incident light into two orthogonally polarized beams, ordinary o- and extraordinary e-rays, with a separation angle of 32.′17 at 6330 Å. This separation angle produces a spatial shift of the two beams that amounts to 11.1 mm at the entrance mask and gives a 3.7-mm separation of the two images at the detector. Therefore, to avoid blending of the o- and e-images, the spatial opening of each slot in the polarimetric mask should be narrower than 10.7 mm, while the gap between neighboring slits should be wider than 10.7 mm in the direction of the beam splitting. Some masks for polarimetry, which have slots with identical sizes aligned at equal intervals, are available for

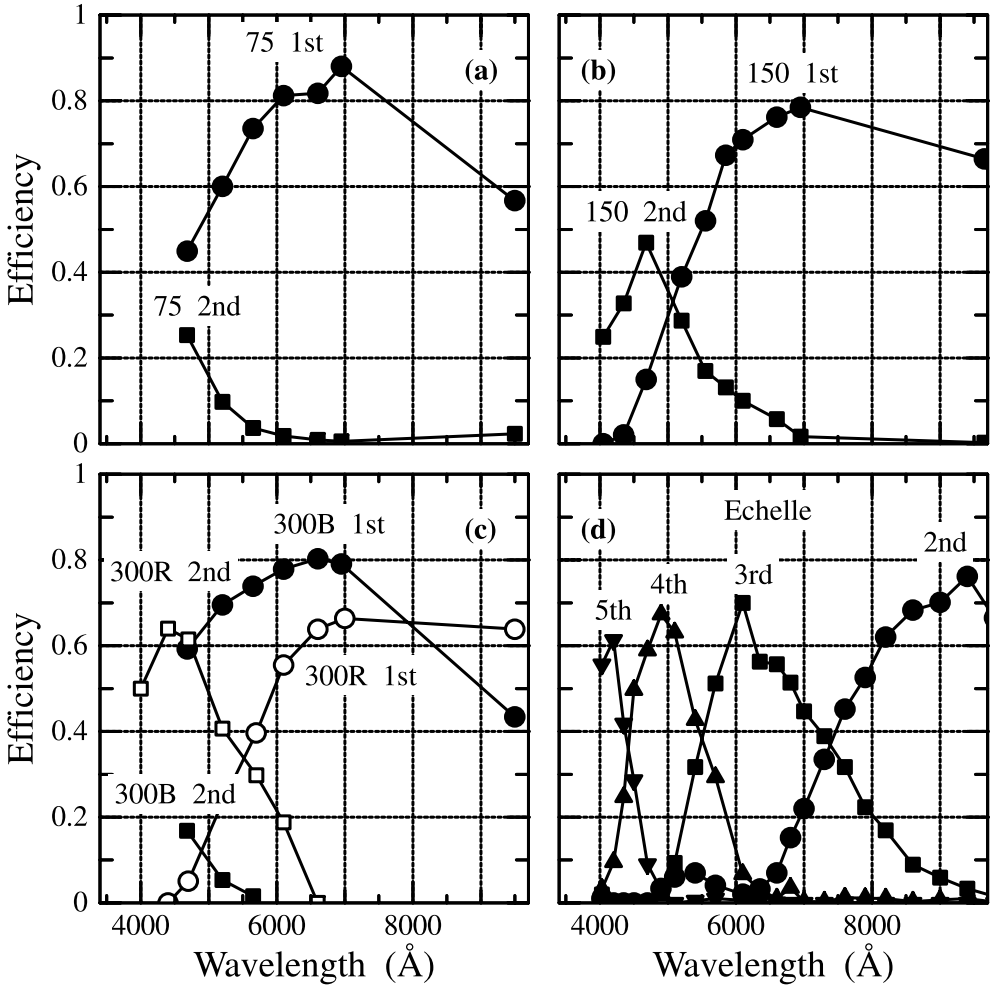

Fig. 5. Measured efficiency curves of the FOCAS grisms: the very low-dispersion grism (upper left panel), the low-dispersion grism (upper right), the blue medium-dispersion grism (lower left), and an echelle-type grism (lower right).

FOCAS. To cover the field of view, it is necessary to take at least three exposures with appropriate shifts of the telescope pointing.

2.4. Image Distortion

For multi-object spectroscopy (MOS) observations, it is necessary to know the accurate positions of the target objects on the slit mask plane or the Cassegrain focal plane of the Subaru Telescope. Therefore, we need to derive the transformation function between the position on the CCDs, measured in pixels, and that on the focal plane, in millimeters. To achieve this, a specially made slit mask with an accurate regular grid of one thousand small apertures was placed on the multi-slit assembly, and the positions of the projected images of the apertures were measured on the CCD. The patterns of the grid images were analyzed to solve simultaneously for the relative positions of the two CCDs (the gap size between the CCDs, the shift in CCD column direction, the relative rotation between the chips, and the distortion center position on the chip) and the optical distortion. Figure 7 is a vector plot, which shows the offsets between the expected grid positions (with no distortion) at the Cassegrain focus and the actual projected positions on the CCD surface, as a function of position over the entire FOV. The coordinates are CCD XY-pixels and the vector to the lower left shows a 5 pix by 5 pix image shift length. The distortion is found to increase with the distance from the center of the FOV. The pattern of the optical distortion is barrel-like and has an amplitude of up to 1.2% at the edges of the FOV. Almost no distortion is seen in the tangential direction. Therefore, the distortion can be simply characterized as a one-dimensional function of the radial distance from the optical center. (This result is not surprising, since the FOCAS optics is linear.) The final radial distortion function can be described with a third-order polynomial function that gives the conversion factor between pixels and millimeters on the mask plane as well as at the center of the FOCAS optics on the CCDs at zenith. The fitting was made with an accuracy of 0.01% of the distortion over the entire field. We found that the pattern holds for any elevation and position angle of the telescope, although the center of the distortion moves because of the flexure of FOCAS. Therefore, it is safe to use these distortion parameters for all telescope pointing. The accuracy of two-chip image-mosaicing, distortion correction, and the pixel scaling ($''$/pix) were checked with six Hipparcos positional standard

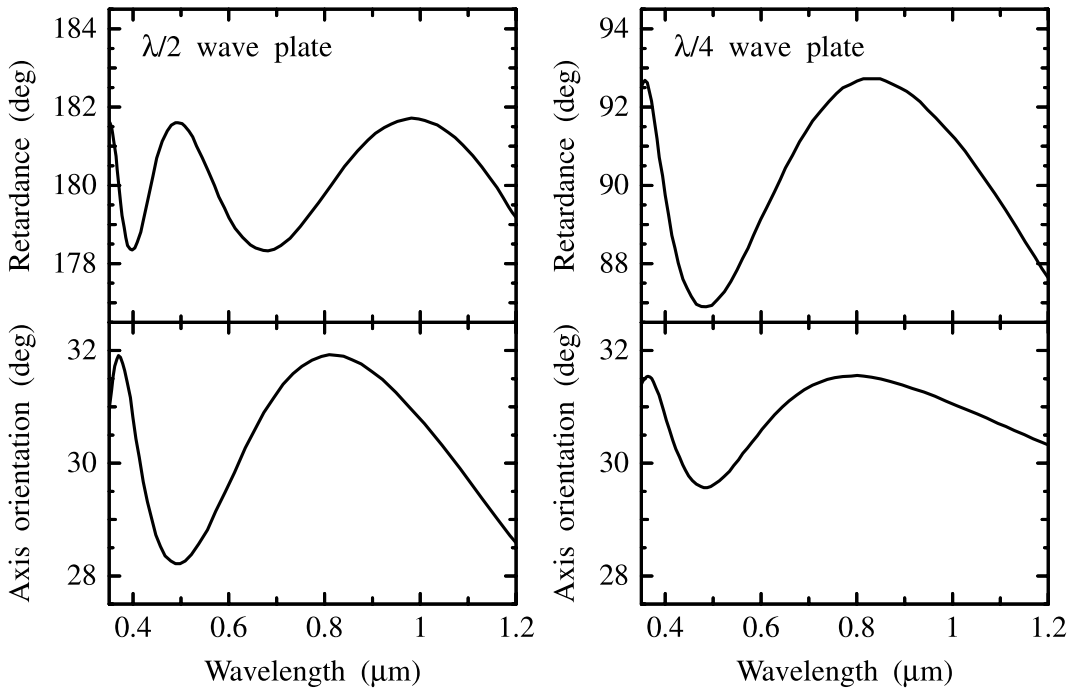

Fig. 6. Specifications of the FOCAS wave plates. The retardance (upper panel) and the orientation of the optical axis (lower panel) are shown for the half-wave plate and the quarter-wave plate, respectively.

Table 1. Set of grisms currently available for FOCAS.

Grisms	R	λ_c (nm)	gr mm^{-1}	Glass	α (deg)
Very low resolution	250	650	75	FK-5	5.75
Low resolution	500	650	150	FK-5	11.55
Middle resolution (blue)	1000	550	300	FK-5	19.72
Middle resolution (red)	1000	750	300	BK-7	26.10

R: spectral resolution with 0.″4 slit width.
λ_c: central wavelength.
α: vertical angle of a prism.

stars, which were distributed across the FOCAS FOV. The positional errors of the distortion-corrected image of these stars were found to be less than 1 pixel (0.″1) over almost the entire 6′ FOV.

3. Mechanics

3.1. Overview

A schematic view of the structure of FOCAS is shown in figure 8. The whole FOCAS instrument has a diameter of 2 m and a height of 2 m, and its weight is approximately 2.1 t. The center of gravity of FOCAS is located in the turret section, which contains some moving parts, such as the grism turret, the three filter turrets, and the two polarizer slides. This turret section is supported by a truss structure from the Cassegrain flange section. This truss support structure is designed to give minimal flexure: this is discussed in more detail below.

FOCAS is attached to the Subaru Telescope by 16 bolts that go through 16 holes in a circular ring on the Cassegrain flange surface by the automatic instrument exchanger (CIAX). The flange section of FOCAS consists of the multi-slit unit, inside the instrument, together with seven external electronic drive units. The 12 trusses are made from CFRP (carbon-fiber-reinforced plastic) which is light (relative density 1.8) and at the same time as strong as Invar (Young's modulus $E = 1.4 \times 10^4$ kg mm^{-2}). Each truss has a diameter of 80 mm and a weight of about 10 kg. The collimator lenses and the camera lenses are integrated in cells that are made of brass. These cells are suspended from the turret section by several limbs attached at their centers of gravity. The lens cells are estimated to be stiff enough to ensure that the maximum displacement due to self-gravity is as small as 0.254 μm for a collimator cell and 1.11 μm for the camera cell. The entire dewar is mounted on an XYZ-stage, which is fixed on the end of the turret section. The focus of the FOCAS, itself, can be adjusted with 3 μm accuracy in this Z-stage.

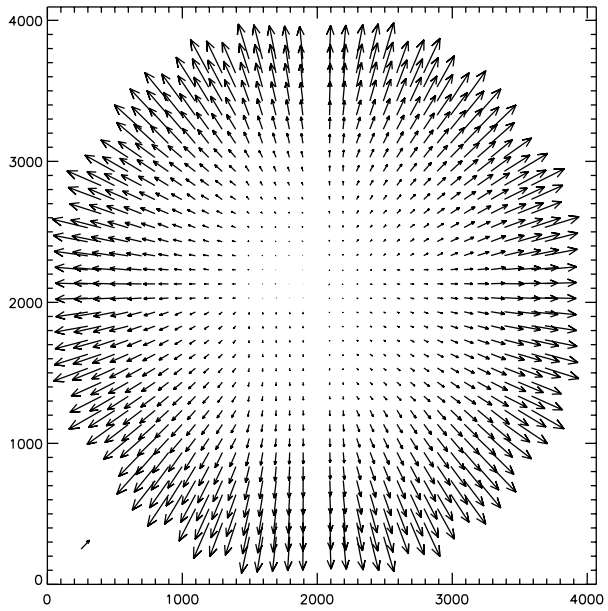

Fig. 7. Vector plot showing the image offsets between the expected grid positions with no distortion at the Cassegrain focus and the actual projected positions on the CCD surface, as a function of position over the entire FOV. The coordinates are CCD XY-pixels and the vector to the lower left shows a 5 pix by 5 pix image shift length.

3.2. Turret Section

Various optical elements, such as grisms, filters, and polarizers, can be inserted in the 451-mm turret section between the collimator lenses and the camera lenses using three turrets or two slides. Figure 9 shows the inside of the turret section: the Cassegrain focus is to the left, and the CCD is to the right. The auxiliary filter turret holds ND filters, Hartman masks for focusing the camera, and calibration filters for polarimetry. A quarter-wave retarder plate and a Wollaston prism are on the slide. Both a half-wave retarder plate and a quarter-wave retarder plate can be mounted on the retarder-plate slide. Rotation of these wave plates is driven by stepper motors with absolute potentiometers, controlled to an accuracy of $\simeq 0.^{\circ}025$. Seven of eight possible positions are available for grisms and filters on each turret. To suppress ghost images produced by reflections internal to the optical surfaces, the filters are tilted by 5° (see figure 2). Each grism and filter can be identified in real time using barcodes attached to their housings. There is also a large turning shutter at the end of the collimated beam. The minimum exposure time is set to be 0.3 s and 3.0 s with 10% and 1% accuracy, respectively. There are access windows in the body surface of the turret section to allow exchange and maintenance of the optical elements.

3.3. Flexure

Low flexure of the instrument is crucial to allow multi-slit spectroscopy using a fixed slit-position mask plate. As the telescope moves from the zenith ($z = 0^{\circ}$) to $z = 80^{\circ}$, the total image shift amounts to 5.5 pix.

However, a typical exposure time would be less than one hour because of contamination due to cosmic rays. In order to obtain good image quality, we require that the image shift should be small over this one-hour exposure, corresponding to a 15° ZD (zenith distance) change. The maximum image shift within this 15° ZD change is 1.3 pix. This image shift, which is larger than the flexures of the collimator/lens cells, themselves (see subsection 3.1), is caused by the truss structure, which keeps the entire optical train in parallel to avoid the image tilts. We have established that any image shift in the direction orthogonal to gravity is negligible at any position angles. The XY-stage in front of the CCD dewar will be used in the future to compensate for any image shift.

A vital point is that the distortion pattern (see subsection 2.4) does NOT depend on ZD to an accuracy of less than 1 pix. That is, the flexure of FOCAS practically causes *only* an image shift. Image distortions must nevertheless be corrected when using the MOS modes, in which a transformation between the Cassegrain focus and the CCD coordinates is essential.

3.4. The Multi-Slit Assembly

The multi-object spectroscopy (MOS) mode over the full $6'\phi$ FOV aims to increase the observational efficiency of spectroscopy, especially for statistical studies. Initially, a direct image must be obtained in order to define the spectroscopic targets. The slit pattern is then designed based on the imaging data. In the future, it may be possible to create a slit pattern based on any astrometric catalog, provided the positions of all the targets are accurately known. The slit masks are manufactured by a slit-mask-making machine (SMMM), which will be described in the next subsection. At the beginning of a spectroscopic observation, the field should be confirmed using bright alignment stars; four or more of these should be found per field. During this plate-alignment procedure, it may be necessary to move the telescope slightly or rotate the plate: after that the telescope can start guiding. Once all of the alignment stars are located just in the center of corresponding holes, we can start an exposure. Three aspects of this MOS procedure require close attention: one is a precise determination of the slit positions; the second is highly accurate slit processing; and the third is a rapid, smooth exchange of the slit masks.

The multi-slit assembly consists of three units: a mask-stacker, a mask-changer, and a mask-stage. The mask-stacker carries up to 10 slit-mask plates at a time. One of the stored plates is taken from the mask-stacker by a vertically moving elevator, and is transported to the focal plane by the horizontal linear guide of the mask-changer. The mask-stage is a precise θ-stage that sets the mask plate with $18''$ rotational position accuracy. If it is necessary simply to shift the mask plate, one can move the telescope, which has a $0.''07$ resolution for pointing accuracy. It takes only 15 s to complete a mask exchange. The long slit mask plates with various slit widths from $0.''2$ to $2.''0$ according to the seeing size or the target size are also installed using this multi-slit assembly.

3.5. The Slit-Mask Making Machine

The slit-masks are manufactured off-line. The slit-mask making machine (SMMM) must cut slits whose width is as fine as 100 μm, corresponding to $0.''2$. The most suitable laser of all those that we investigated was a diode-pumped YAG laser, ML-7040A, made by Miyachi-Technos Co. This is a

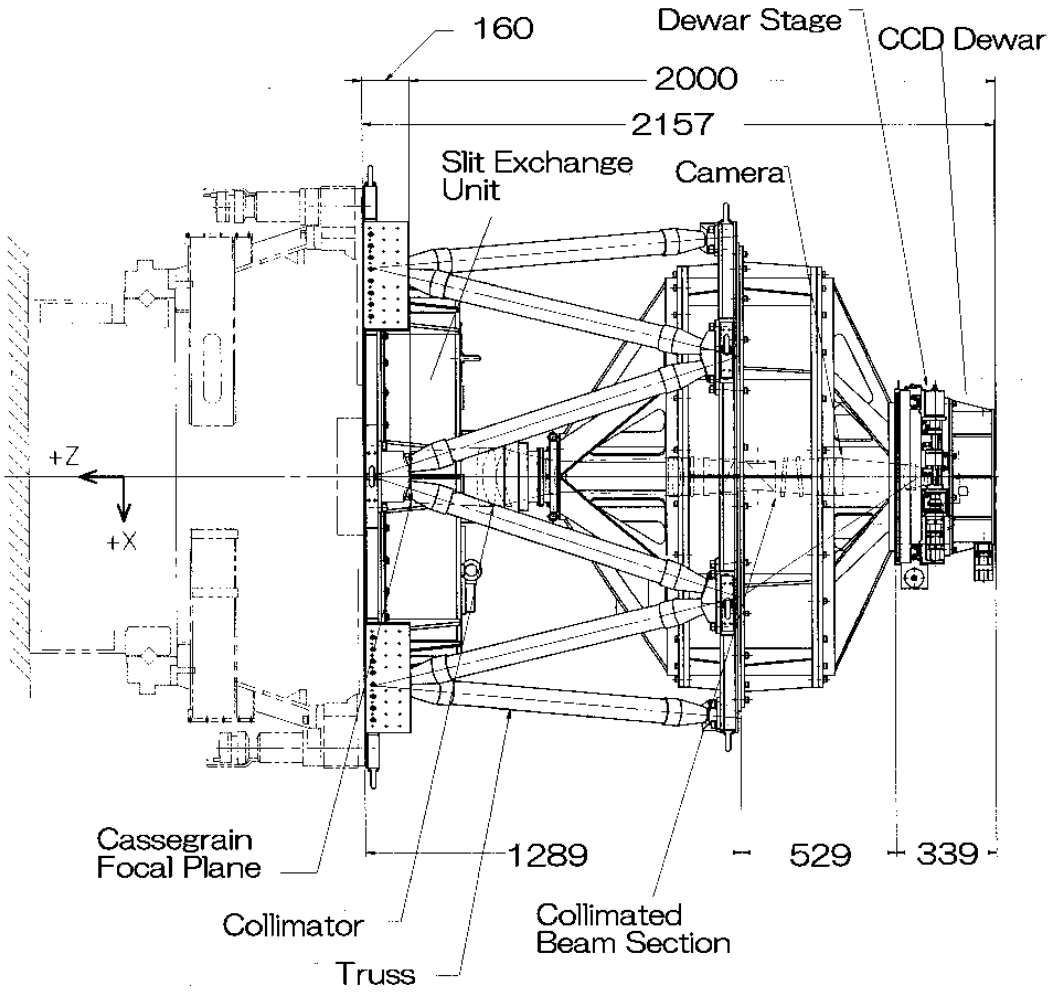

Fig. 8. Overview of FOCAS. The Subaru Telescope is to the left.

compact system, and is cooled only by circulation of the primary coolant. The laser, itself, is a multi-mode, Q-switched pulsed system, operating at a wavelength of 1064 nm, and has a power as high as 15 W. The SMMM also has a precise XY-stage to carry the slit-mask plate. The system is designed to give the position accuracy of slits as small as 1 μm. The straightness of the slit edge is 8 μm r.m.s., and parallelism error of slit edges is $0.^{\circ}002$. The SMMM can cut slits which have widths larger than $0.''2$, though the mask positioning error is $0.''2$ at most. To avoid flexure and thermal expansion, the slit mask is made of four multi-layered carbon-fiber sheets, 100 μm thick. Though this flat slit mask is located on the Cassegrain focus, which has a spherical curvature, the difference in the best focus position between at the field center and at the field edge is less than the focal depth. Determination of the precise positions of the slits from imaging data is carried out by the software described in subsection 5.5.

4. The CCD Camera

The FOCAS CCD camera consists of a pair of abuttable CCDs of 2048 $\times$ 4096 pixels with 15 μm-square pixels. The CCD chips were fabricated by MIT. The quantum efficiency of the CCD is presented in Miyazaki et al. (2002). The CCDs cover the entire Subaru Cassegrain $6'$-diameter FOV, and the pixel scale is $0.''103$/pix, which yields good sampling of the image at the best seeing size available at the summit of Mauna-Kea.

The CCDs are placed in a dewar of size 200 mm (diameter) $\times$ 100 mm (height). The AlN motherboard on which the CCD chips are mounted is supported by four polycarbonate posts and is thermally isolated. The CCDs are cooled to $-100\,^{\circ}$C with a WE-5000A Stirling cycle cooler manufactured by DAIKIN Co. We usually use this cooler at the 65% output level. The motherboard is connected to the head of the cooler by so-called 'cold fingers', made of copper straps, which almost absorb the vibration of the cooler compressor. The maximum image smearing caused by this vibration is estimated to be less than 0.1 pix, which corresponds to 2.5% image degradation under the best seeing size of $0.''4$.

The method of CCD mosaicing was essentially the same as that used by Sekiguchi et al. (1992) and Miyazaki et al. (1998). Each chip was mounted on a finely machined Invar spacer, which was matched to the material of the CCD package. We

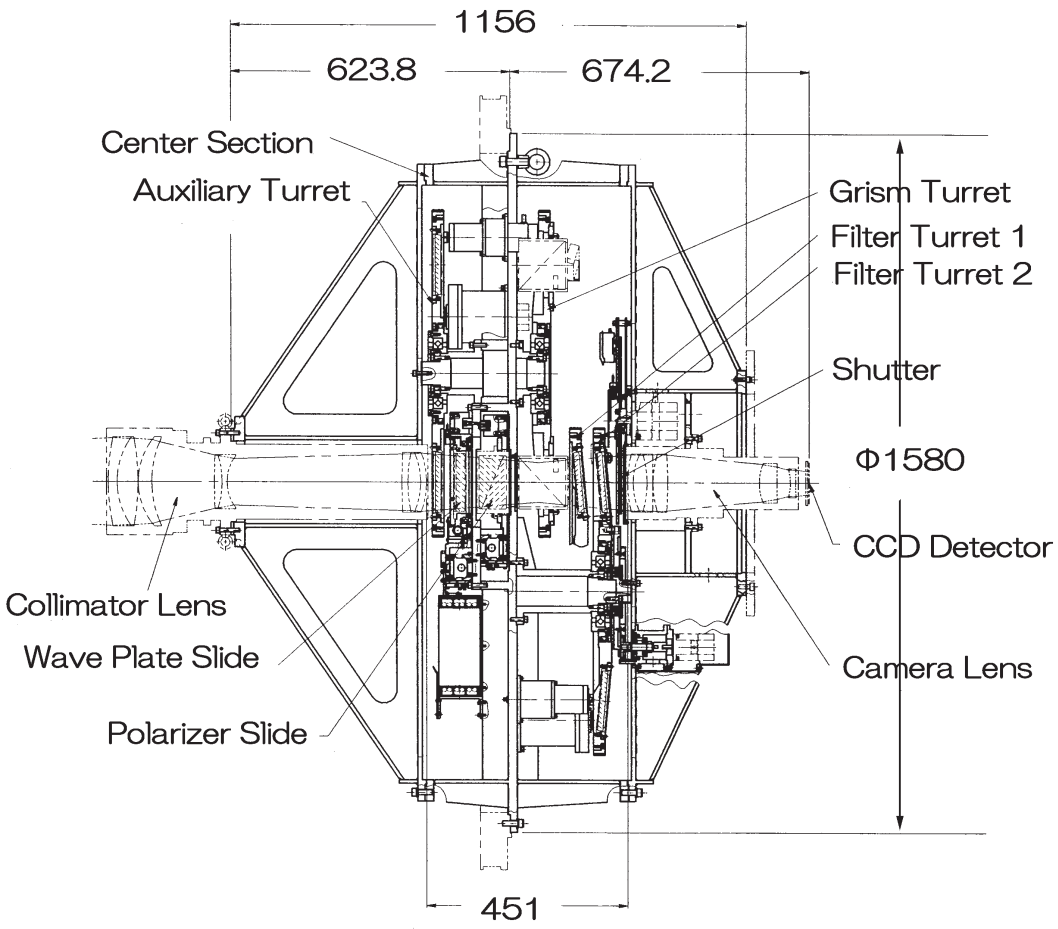

Fig. 9. Internal view of the FOCAS turret section. The Cassegrain focus is to the left and the CCD is to the right.

glued each CCD chip onto the spacer under a microscope, using a laser displacement meter to measure the x–y positions and the height. The glue was an Ag-based conductive epoxy. Thin metal shims were inserted between the chips and the spacer to ensure that the thickness of the glue was even. We then screwed the CCD chip and the spacer onto an AlN motherboard, using a microscope for accuracy. The size of the gap between the two CCD chips is 50.35 pix and the misalignment of the CCD rows is 1.805 pix. The tilt angle of the chips with respect to each other is $0.^{\circ}005183$, which corresponds to a 0.36-pix deviation over the 4000 pix of the CCD. The height difference of the two CCD chips is estimated to be $10\,\mu$m, which is much smaller than the focal depth ($50\,\mu$m).

We use a system called Messia III (Modularized Expandable SyStem for Image Acquisition: Sekiguchi et al. 1996) and MFront (Mosaic CCD Front-end electronics) for CCD control and data acquisition. These are the standard optical-CCD controllers for the Subaru Telescope. Messia III is based on a VME bus, and was originally designed for operation with a single chip. The two CCDs are read out simultaneously. The front-end electronics inside the dewar contain two channel switches, which generate the clock and FET amplifiers. The amplified analog signals are sent to 16-bit A/D converters, which are located outside the dewar, as close as possible to the CCDs. It takes about 98 s to read all the effective pixels in the 1×1 binning mode. The conversion factor of the CCD chips is $1.9\,e^{-}$/ADU. The CCD operation and data acquisition software are part of FALCON (Yoshida et al. 2000, and see below).

4.1. Performance

The response to the input light flux is linear in the range 0 to $40000\,e^{-}$ with a 0.5% r.m.s. fluctuation. The readout noise is 4.1–5.1 ADU, which corresponds to 9–$10\,e^{-}$. Although the bias level shows some chip-to-chip variance, it is quite stable, with the amplitude fluctuations being smaller than the readout noise once 10 minutes have elapsed since digital power-up. The dark current is negligible at CCD temperatures of $-90\,^{\circ}$C to $-100\,^{\circ}$C.

5. Control System

5.1. System Overview

The configuration of the FOCAS control system (Sasaki et al. 1997; Yoshida et al. 2000) is shown in figure 10.

The motor drive units directly drive the motors of the FOCAS devices and receive the output from the devices' encoders. Local control units (LCUs), which are one-chip microcomputer boards, control the devices through the motor drive units. LCUs also control the barcode readers, the power to the CCDs, the cooler, and the insulator valve. A VME board

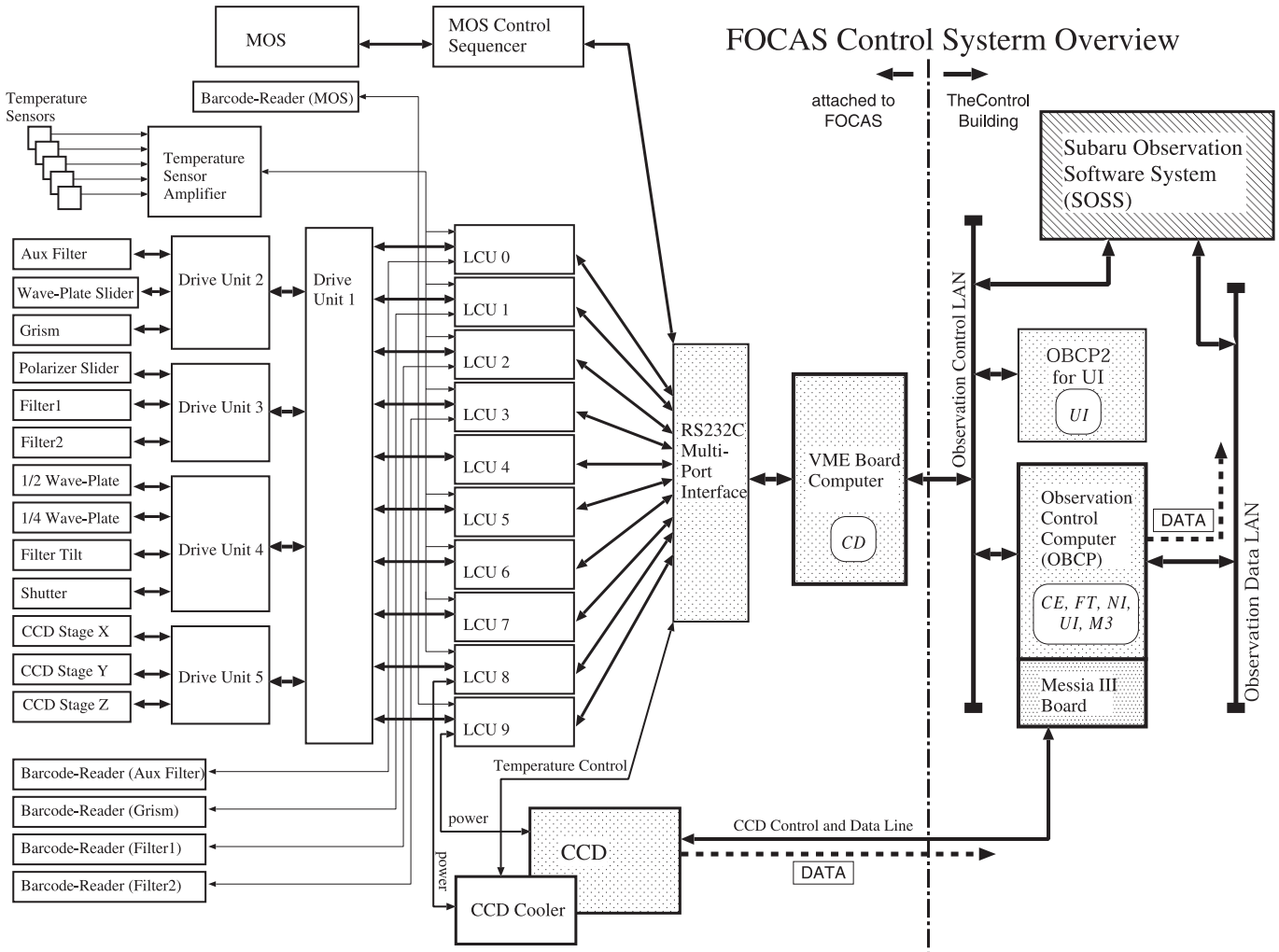

Fig. 10. FOCAS control system overview. This figure shows mainly the hardware configuration of the system. The components shown on the left-hand side of the dot-dashed line are attached to the instrument, whereas the components on the right-hand side are installed in the control building of the Subaru Telescope. CCD image data are sent to the OBCP from the CCD controller through a high-speed optical fiber channel.

computer, which is installed in a thermal insulation box, is the host computer for the LCUs. All the LCUs are asynchronously controlled by the host computer through a multi-port RS232C interface. The VME board computer also communicates with the sequencer of the multi-slit exchange system through one of the RS232C ports, and controls the multi-slit assembly. The observation control computer (OBCP) of FOCAS is in the control building of the Subaru Telescope, and the main part of the control software of FOCAS runs on this machine. The CCDs are directly controlled by the OBCP using the Messia III system. The CCD data are transferred to the OBCP through a high-speed optical fiber channel and are stored in a shared memory region of the OBCP. The whole system is connected by a network to the Subaru Observation Software System (SOSS) (Kosugi et al. 1997; Sasaki et al. 1998).

5.2. Hardware

5.2.1. Drive units

The motor drive units of FOCAS were developed by NIKON Co. Five drive units, one master and four slaves, are attached to FOCAS.

5.2.2. Local control units (LCUs)

The LCUs are custom-made one-chip microcomputer (H8/3048F-ZTAT) boards. The LCU's built-in software is installed into the rewritable ROM of the CPU. The software provides a simple command protocol (hereafter 'LCU-command'), which is used for communication between the LCUs and the host computer. All of the movable devices of FOCAS, except for the multi-slit assembly, can be monitored and controlled by sending LCU-commands to the LCUs via the RS 232C interfaces. A single LCU is able to control several devices simultaneously, and also monitors the temperature sensors that are installed at various points in FOCAS.

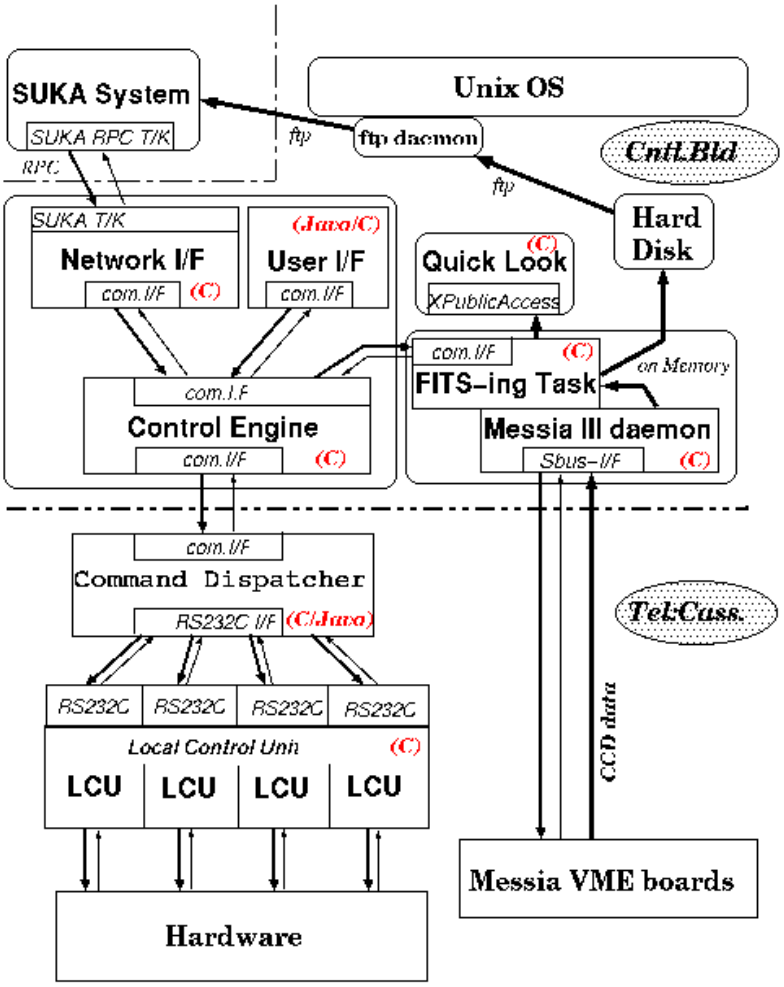

Fig. 11. FALCON internal structure. Commands input from the UI or the SOSS through the NI are transmitted to the CE. The CE checks the commands and dispatches them to the appropriate processes, CD, M3, or UI.

5.2.3. Thermal insulation system

The thermal insulation system, which consists of thermal insulation boxes in which the motor drive units, the VME rack, and the multi-slit assembly controller are stored, was constructed by THK Co. All of the insulation boxes are connected in parallel with the coolant pipeline, and each one has an automatic air valve, which controls the coolant flow. The valve opens when the internal temperature of the insulation box is higher than the external temperature, and closes when the internal temperature is more than five degrees below the external temperature.

5.2.4. Environment monitors

FOCAS has 33 temperature sensors, an air-pressure monitor, a vacuum monitor for the CCD dewar, and a CCD-temperature sensor.

5.3. FALCON

5.3.1. System overview

The instrument control software of FOCAS (FALCON; FOCAS all-round control software) (Sasaki et al. 1997; Yoshida et al. 2000) was designed to be a network-distributed, multi-process system. It consists of several internal processes: a network interface (NI) process, a user interface (UI) process, a central control engine (CE) process, a command dispatcher (CD) process, the local control units (LCUs), the Messia III (M3) daemon process, and a data FITS conversion task (FT). The structure of FALCON is shown in figure 11.

Each process can be run independently, and communicates with other processes by passing command strings using Sun RPC (remote procedure call). In the following section we briefly describe the format of the command strings.

5.3.2. FALCON internal commands and control objects

A FALCON internal command (hereafter FALCON-command), used in communications between the internal

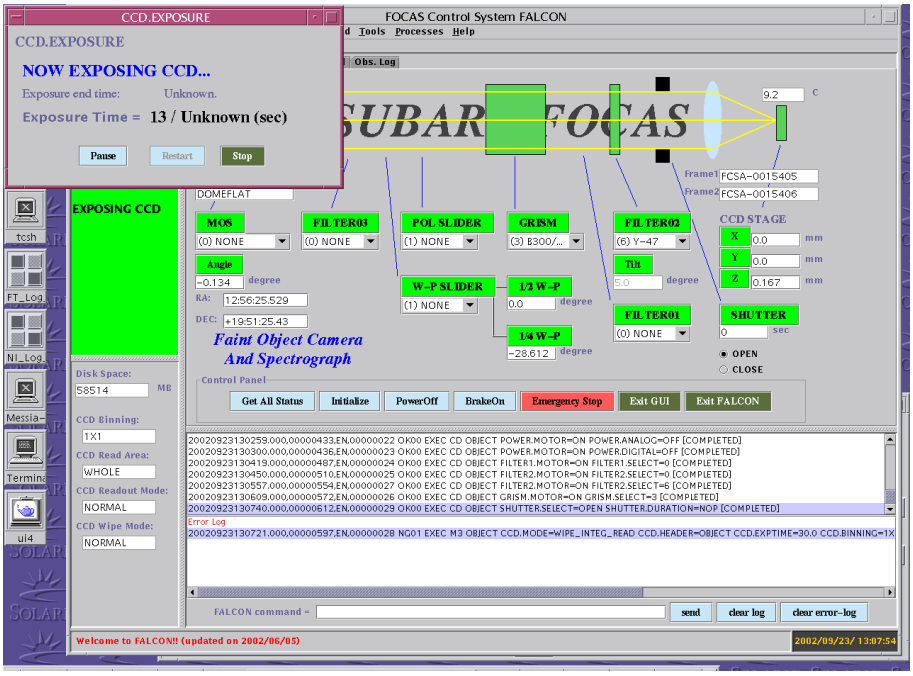

Fig. 12. Main panel of the FALCON user interface (UI).

processes of FALCON, is composed of a fixed-length (69-byte) header and a command sentence. The header contains the total length of the command, the date and time, the sequential number of the command, the name of the command transmitting process, and the name of the command destination process. A command sentence is variable in length, and is composed of a verb, a destination process/instrument, a command object, the control objects, and the parameters of the control objects.

5.3.3. Individual processes

(a) Command Dispatcher (CD)

CD lies above LCU in the FALCON hierarchy. CD receives FALCON-commands from the CE, analyzes them and translates them into LCU-commands, then dispatches the commands to the appropriate LCUs. It also maintains the execution status of received FALCON commands and the status of the devices of FOCAS. CD has an internal command-dispatcher thread, a status-management thread, a command-execution watcher, network-interface threads, and RS232C-interface threads. Those threads run in parallel and communicate with each other through internal command buffers.

(b) Messia III Daemon (M3)

M3 acts as the interface between the Messia control software (Sekiguchi et al. 1996) and the CE. The Messia control software controls the general-purpose CCD control system, Messia III. M3 adds an RPC interface at the command input gate of the Messia software, and receives the responses from the Messia through a pipe. In addition, M3 controls the CCD exposure processes; i.e., shutter control, wiping the CCD (reading out the residual electrons from the CCD), and CCD readout.

(c) FITSing Task (FT)

After a CCD readout has been completed, the read-out data are stored in a region of shared memory on the OBCP. FT reads the data in the shared memory and creates a FITS file containing the telescope and instrument status. The telescope status is retrieved from the SOSS through the CE process and the NI process. The instrument status is obtained from CD through the CE.

(d) User Interface (UI)

The UI is written in Java with Swing API (figure 12). Since the source code of the UI is pure Java, the compiled byte code of the UI can be run on any platforms that support JDK 1.1 or later. The UI displays the complete instrument status and the command execution status, as notified by the CE. All of the FOCAS devices can be controlled using the UI. The UI also communicates with FALCON by RPC. This thin connectivity to the main engine of the software, together with the platform-independent characteristics of Java, make the UI highly portable.

(e) Network Interface (NI)

The NI interfaces FALCON with the SOSS. The NI consists of the SOSS interface toolkit and a translator between the SOSS commands and FALCON commands.

(f) Control Engine (CE)

The CE supervises and harmonizes all of the processes running in FALCON. It carries out format checking and grammatical checking of input commands, and dispatches them to the appropriate processes. It maintains a record of the running status of each process, and the status of the instrument reported by CD. In fully functional, normal operation mode, the processes in FALCON communicate with each other through the CE (see figure 11).

5.4. Control Sequence — Command Flow in FALCON

The outline of the command flow in FALCON is as follows. A FALCON-command input from the UI or the SOSS is initially transmitted to the CE. The CE checks the command for format and grammatical errors, and then checks the validity of the control objects and their parameters indicated in the command sentence. If the command is valid, the CE sends it to the appropriate process. The process receiving the command executes it and returns a completion message to the CE when the execution is ended. The CE then notifies the UI and the SOSS of command completion.

Under normal operation mode, FOCAS is controlled from the SOSS. In order to achieve a high observation efficiency, "observation abstract commands" (Kosugi et al. 1997) can be defined by instrument developers or users in the SOSS. An abstract command is a macro command representing an observation sequence.

As described in subsection 5.1, CCD data obtained by the Messia III system is transmitted to a shared memory region of the OBCP by M3, and is translated into FITS by FT. Afterwards, the SOSS transmits the FITS file to the Subaru data archive system.

6. User Support Software

6.1. Data Reduction Software

We have developed a software package within IDL for the special data reduction procedures required for FOCAS. The software combines the two CCD images into a single large image, while correcting for the CCD positional offsets and the optical distortion. The image re-formatting is carried out by dividing pixel counts into four neighbor pixels, according to the position of the new pixel coordinates calculated from the distortion pattern. Simple bias subtraction and flat-fielding are also possible within this software to allow a quick check of images during observations.

In addition, a similar software package for spectral images has been developed. It straightens out the distorted spectral image (with an arc-like bend in the space direction), taking account of the wavelength-dependence of the optical distortion. The distortion of the spectrum can then be further reduced in the dispersion direction with a two-dimensional spectral fitting program, like the **`reidentify`**, **`fitcoord`**, and **`transform`** tasks implemented in IRAF. The main part of these programs (the part without a FITS I/O interface) can also be used as the processing engines in the DASH software environment.

6.2. FOCAS Setup Software

In addition to providing software to deal with a distortion correction, we have also developed a software package to support the regular maintenance of FOCAS. This software is used for checking the alignment between the grism or long-slit and the CCD columns and rows, for checking the CCD rotation, and for focusing the FOCAS camera and telescope. The program traces images, either of the continuum spectrum of point sources aligned in a straight line (made by pinholes on the slit mask) or a direct image of the long slit, and calculates the angular offset between the image and the CCD column/row. Focusing of the camera is performed using a Hartmann test; the software compares a set of spectra of the calibration HCT lamp taken with different Hartmann shutters installed in the auxiliary turret, and calculates the focus offset based on the calibration curve, which relates the CCD Z position to the differences between the same lines taken with different Hartmann filters.

Quick focusing of the telescope is usually carried out with the telescope's own auto-guiding camera. However, the best focus position can be measured using the FOCAS image, itself, by taking a multi-exposure image of stars while changing the telescope focus positions. The software can then calculate the best focus positions by fitting to the stellar images and the focus values. All of these software packages are coded within the IDL environment, and provide graphical interfaces for easy and quick data analysis. These packages, and other software, such as the MOS pointing and distortion correction programs, can be easily launched from a command launcher, which is another graphical user interface program written in IDL.

6.3. Mask Design Program

For an efficient arrangement of the slits on the mask, we have developed a dedicated piece of software, the Mask Design Program (MDP) (figure 13). The goal of this program is to take the object list provided by the observer and make a slit list that describes the slit positions (in mm) on the mask plane, which can then be used in fabricating the slits with SMMM. Currently, an image taken with FOCAS is required for the mask design process, since we use the transformation function between the slit mask and the CCD plane based on an analysis of the grid mask images (see subsection 2.4). The object list contains information on the target positions (X–Y positions of the target in pixels) and the shape of the slit (length/width of the slit in pixels) as well as the slit priority. MDP has the following features for efficient mask design:

1. Assigned slit positions and regions occupied by the spectrum of each slit (including nth-order light positions) are shown graphically, superposed on a direct image.
2. Circular apertures for alignment stars can also be created.
3. It provides an interactive interface for modifying the slits (i.e., adding and deleting some slits, changing slit length, and so on) in the case of overlaps between the spectra. The software presents a warning message if such overlaps are expected. Rejection of slits with lower priority is also possible, if the priority has been properly specified in the object list.
4. It helps to prevent target objects from falling into the gap between the two CCDs, or out of the FOV.
5. It is possible to change the center of the object if the desired targets are imaged towards the edge of the FOV, or if bigger images with a larger FOV made from several dithered images are used.

6.4. Slit Mask Alignment Software

Accurate alignment of the slit mask on the sky is performed by another dedicated piece of software, which automatically

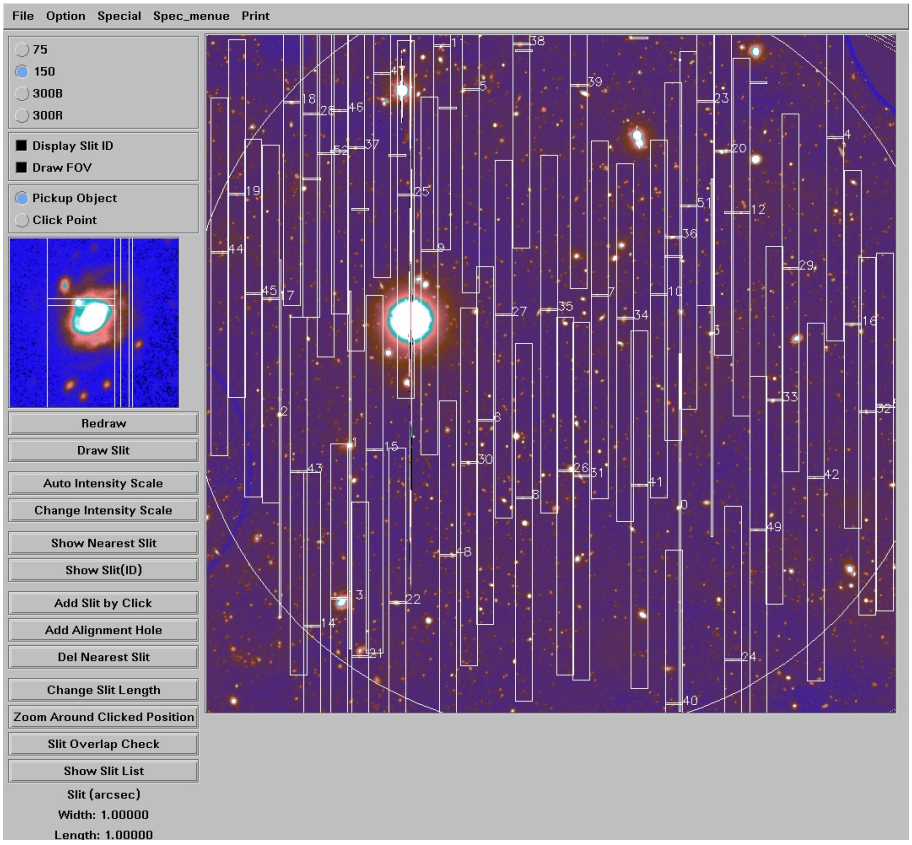

Fig. 13. Mask Design Program.

derives both the telescope offsets (in right ascension [RA] and declination [DEC]) and the rotation of the mask. These offsets are calculated based on the positions of the apertures on the mask and of corresponding alignment stars on a direct image. First, the aperture positions are measured based on a short exposure image with the slit mask inserted in the focal plane. Next, a direct image of the target field is taken with the mask off. The software compares the aperture and alignment star positions in these two images, and then derives the telescope offsets and the mask rotation angle after correcting for any optical distortion. After moving the telescope in RA and DEC and rotating the slit mask, the next image is taken with the slit mask in. This time, most of the alignment stars would be expected to come into the alignment apertures, and the aperture and star positions are measured again with this single image to confirm the alignment star positions. If more precise pointing is required, one may take another image with the slit in place, and repeat the above procedure until the required pointing accuracy is achieved. The time required for this MOS pointing is 15–30 min, depending upon the number of iterations made during the procedure described above. We often use at least four alignment stars, two on each CCD chip, since the residuals of the aperture–star positions give an estimate of the slit positioning accuracy, which includes errors not only in the pointing, but also in the distortion measurement and the CCD alignment. The typical maximum positioning error is found to be less than 2 pixels ($< 0\farcs2$) and the r.m.s. error is less than 1 pixel ($< 0\farcs1$) across the FOV.

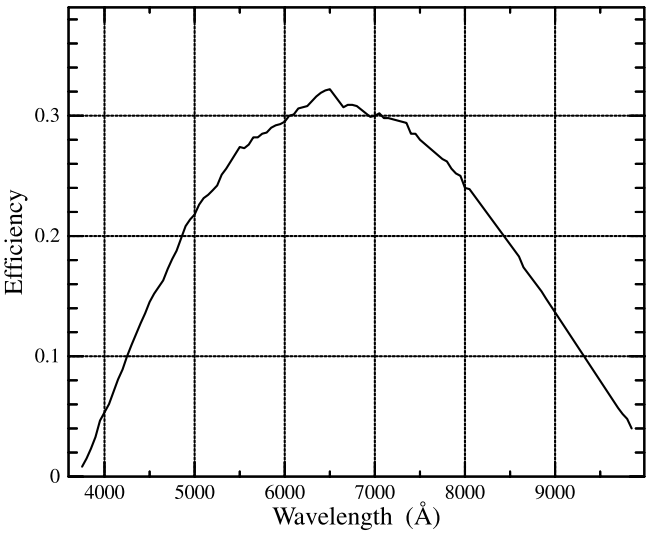

Fig. 14. Measured efficiency of FOCAS, including the throughput of the telescope, ADC, FOCAS optics, and the detector efficiency.

7. Performance

7.1. Limiting Magnitudes

We calculated the limiting magnitudes of FOCAS using observations of photometric standard stars (Landolt 1992). We assumed a point source located at the zenith on a dark night.

The sky brightness was 21.9, 21.1, 20.5, and 19.5 mag arcsec^{-2} in B-, V-, R-, and I-band, respectively. We took the readout noise to be 10 electrons in the 1×1 binning mode. The aperture size in photometry was assumed to be $2''.0$ diameter when the seeing was $0''.5$ FWHM. We found limiting magnitudes of a 1200-s exposure with S/N = 3 to be 26.9, 26.5, 26.2, and 25.5 mag in the B-, V-, R-, and I-band, respectively.

7.2. *Throughput*

We measured the throughput of FOCAS attached to the Subaru Telescope by observing spectrophotometric standard stars. The stars G191B2B and Feige 110 (Massey et al. 1988; Massey, Gronwall 1990) were used as the standards. They were observed with a $2''.0$ width slit under $0''.5$–$0''.8$ seeing conditions. The whole spectral range from 3800 Å to 10000 Å was covered with multiple-order cut filters. The throughput, which is defined as the ratio of the number of electrons produced by the CCD to the number of photons gathered by the telescope, is shown in figure 14 for the 300 (blue) grism. The throughput shown in figure 14 was measured through the Cassegrain atmospheric dispersion corrector (ADC), made of a pair of rotating double prisms with oil contact to minimize the reflection loss (Wynne, Worswic 1986).

We would like to thank all of the present and former staff of the Subaru Telescope for their invaluable help in commissioning the FOCAS. We wish to thank T. Ezaki, S. Tsuda, T. Nishioka, K. Obata, A. Hirota, E. Miyano, K. Mukai, K. Ishibashi, and A. Shiki of NIKON, Co.; Y. Komine, and A. Tokuda of KNT, Co.; T. Fujimaru, and late Y. Eshita of Seikousya, Co.; H. Nita, and M. Sugita of Japan Laser, Co.; and the following NAOJ collaborators: Y. Kamata, H. Kataza, Y. Komiyama, N. Okada, K. Omata, Y. Mikami, S. Miyazaki, T. Nishimura, T. Nishino, M. Sekiguchi, N. Takato, T. Noguchi, T. Usuda, T. Yamashita, and M. Yutani. We thank the referee, Walter Seifert, for his useful comments and suggestion that have improved our paper. This project was supported in part by the Japanese Ministry of Education, Culture, Sports, Science and Technology through Grant-in-Aid No. 11691140.

References

Ebizuka, N., Kobayashi, H., Hirahara, Y., Wakaki, M., Kawaguchi, K., Sasaki, T., & Iye, M. 2000, in ASP Conf. Ser. 195, Imaging the Universe in Three Dimensions: Astrophysics with Advanced Multi-Wavelength Imaging Devices, ed. W. van Breugel & J. Bland-Hawthorn (San Francisco: ASP), 564

Iye, M. 1994, Proc. SPIE, 2198, 153

Kaifu, N., Usuda, T., Hayashi, S. S., Itoh, Y., Akiyama, M., Yamashita, T., Nakajima,Y., Tamura, M., et al. 2000, PASJ, 52, 1

Kashikawa, N., Inata, M., Iye, M., Kawabata, K., Okita, K., Kosugi, G., Ohyama, Y., Sasaki, T., et al. 2000, Proc. SPIE, 4008, 104

Kosugi, G., Sasaki, T., Aoki, T., Kawai, J. A., Koura, N., & Kusumoto, T. 1997, Proc. SPIE, 3112, 284

Landolt, A. U. 1992, AJ, 104, 340

Massey, P., & Gronwall, C. 1990, ApJ, 358, 344

Massey, P., Strobel, K., Barnes, J. V., & Anderson, E. 1988, ApJ, 328, 315

Miyazaki, S., Komiyama, Y., Sekiguchi, M., Okamura, S., Doi, M., Furusawa, H., Hamabe, M., Imi, K., et al. 2002, PASJ, 54, 833

Miyazaki, S., Sekiguchi, M., Imi, K., Okada, N., Nakata, F., & Komiyama, Y. 1998, Proc. SPIE, 3355, 363

Sasaki, T., Iye, M., Yamashita, T., & Shibata, T. 1994, Proc. SPIE, 2198, 322

Sasaki, T., Kosugi, G., Noumaru, J., Takata, T., Mizumoto, Y., Ogasawara, R., Chikada, Y., Tanaka, W., & Kawai, J. A. 1998, Proc. SPIE, 3349, 427

Sasaki, T., Yoshida, M., Shimizu, Y., Kosugi, G., Kashikawa, N., Yadoumaru, Y., Takata, T., & Iye, M. 1997, Proc. SPIE, 3112, 267

Sekiguchi, M., Iwashita, H., Doi, M., Kashikawa, N., & Okamura, S. 1992, PASP, 104, 744

Sekiguchi, M., Nakaya, H., Kataza, H., & Miyazaki, S. 1996, in Proc. Optical Detectors for Astronomy, 157

Wynne, C. G., & Worswick, S. P. 1986, MNRAS, 220, 657

Yoshida, M., Shimizu, Y., Sasaki, T., Kosugi, G., Takata, T., Sekiguchi, K., Kashikawa, N., Aoki, K., et al. 2000, Proc. SPIE, 4009, 240